CrossMark

# MagneDyn: the beamline for magneto dynamics studies at FERMI

Cristian Svetina,[a,b]* Nicola Mahne,[a] Lorenzo Raimondi,[a] Antonio Caretta,[a] Barbara Casarin,[a] Martina Dell'Angela,[a] Marco Malvestuto,[a] Fulvio Parmigiani[a,c] and Marco Zangrando[a,d]

[a]Elettra-Sincrotrone Trieste SCpA, SS 14 km 163.5 in Area Science Park, 34149 Basovizza, Italy, [b]Graduate School of Nanotechnology, University of Trieste, Piazzale Europa 1, 34127 Trieste, Italy, [c]Department of Physics, University of Trieste, Via A. Valerio 2, 34127 Trieste, Italy, and [d]IOM-CNR, Laboratorio TASC, SS 14 km 163.5 in Area Science Park, 34149 Trieste, Italy. *Correspondence e-mail: cristian.svetina@elettra.eu

The future Magneto Dynamics (MagneDyn) beamline will be devoted to study the electronic states and the local magnetic properties of excited and transient states of complex systems by means of the time-resolved X-ray absorption spectroscopy technique. The beamline will use FERMI's high-energy source covering the wavelength range from 60 nm down to 1.3 nm. An on-line photon energy spectrometer will allow spectra to be measured with high resolution while delivering most of the beam to the end-stations. Downstream the beam will be possibly split and delayed, by means of a delay line, and then focused with a set of active Kirkpatrick–Baez mirrors. These mirrors will be able to focus the radiation in one of the two MagneDyn experimental chambers: the electromagnet end-station and the resonant inelastic X-ray scattering end-station. After an introduction of the MagneDyn scientific case, the layout will be discussed showing the expected performances of the beamline.

## 1. Introduction

Magnetism is an essential feature of the macroscopic world. Nowadays, advanced applications of magnetic phenomena are at the bases of the widespread technology underlying magnetic storage, quantum computing, spintronics and energy recovery, which have fuelled a renaissance in magnetism research (Stohr & Siegmann, 2006). At the moment one of the most fascinating aspects in magnetism is the ultrafast disappearance, creation and control of magnetic states and the novel dynamical quantum magnetic effects, which emerge in two-, one- and zero-dimensional systems (Bigot et al., 2009; Tudosa et al., 2004). Correspondingly, a central problem in modern magnetism research is the understanding of the magnetization in out-of-equilibrium excited states (Kirilyuk et al., 2010). Such states, typically initiated by changes in temperature, optical excitations, fields (charge currents) or spin currents, define the operational processes and timescales in magnetic devices. Their understanding is therefore of paramount importance from both a scientific and a techno-logical perspective. However, due to this strong non-equili-brium state, the conventional description of magnetic phenomena in terms of thermodynamics, namely the magnetic precession described by an adiabatic approach through the Landau–Lifshitz equations, is no longer valid. As a result, the ultrafast channels for transferring energy and angular momentum between photons, electrons, spins and phonons remain elusive and a subject of intense debate. For example,
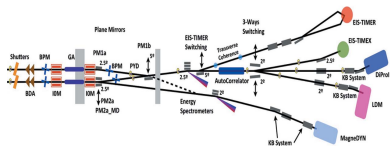
theoretical explanations of the ultrafast demagnetization have been suggested, but the underlying mechanism is not fully understood. Models such as phonon-assisted Elliot–Yafet spin flip (Carpene *et al.*, 2008; Cinchetti *et al.*, 2006; Koopmans *et al.*, 2005, 2010; Stamm *et al.*, 2007; La-O-Vorakiat *et al.*, 2009), electron–magnon scattering processes (Carpene *et al.*, 2008), superdiffusive transport (Battiato *et al.*, 2010) and, more recently, dynamic exchange splitting (Mueller *et al.*, 2013) have been proposed. All these approaches capture only partially the faceted aspects of non-adiabatic spin dynamics, revealing the complexity and the difficulty in describing a ferromagnetic system under strong optical excitation. Consequently, the multidimensional and simultaneous observations of different degrees of freedom, which compete to originate the out-of-equilibrium magnetic phenomena, are now mandatory and will unlock the gate to the non-equilibrium exotic physics of ultra-fast magnetism. The fact that many fundamental aspects of the nature of magnetism occur in the sub-picosecond time regime (Beaurepaire *et al.*, 1996) combined with the intrinsic sensitivity of circular polarized photons as a tool to investigate basic components of magnetism in matter (Boeglin *et al.*, 2010; Stamm *et al.*, 2007; Wietstruk *et al.*, 2011) makes FERMI a versatile state-of-the-art light source for topical research on magnetism. In general, the FERMI free-electron laser (FEL), with coherent high-brightness circularly polarized X-rays at energies resonant with the $3d$–$4d$ transition metal ions, will permit the investigation in real time of fundamental magnetic interactions such as the exchange interaction, responsible for the existence of magnetic order, and spin–orbit interactions.

The MagneDyn initiative aims at combining the unprecedented and unique properties of the FERMI FEL light with complementary X-ray and optical spectroscopies, which have been demonstrated to be effective tools to access different aspects of magnetic phenomena, such as spin and orbital angular momenta [X-ray magnetic circular dichroism (XMCD)], low-lying magnetic, orbital and charge excitations [resonant inelastic X-ray scattering (RIXS)], magneto-optical and non-thermal photomagnetic effects [magnetic optical Kerr effect (MOKE)]. The MagneDyn beamline will deliver FEL light to two experimental end-stations: the first station, equipped with a 2 T electromagnet and a 10 K cryomanipulator, will be dedicated to combined XMCD and MOKE experiments; the second end-station, which is provided with a commercial X-ray emission spectrometer, will be devoted to RIXS experiments.

## 2. FERMI

FERMI is the first single-pass seeded FEL user facility. It is based on the principle of the high-gain harmonic generation (HGHG) (Yu, 1991) scheme, providing transform-limited highly brilliant ultra-short pulses with narrow bandwidths in the VUV–soft X-ray range. It is endowed by two separate sources: the low-energy branch, named FEL1 (Allaria *et al.*, 2010, 2012), covering the wavelength range from 20 nm up to 100 nm (15–62 eV), and the high-energy line, FEL2, covering

**Table 1**
Main output parameters measured at FERMI during the commissioning of both FEL1 and FEL2.

|  | FEL1 | FEL2 |
|---|---|---|
| Wavelength (nm) | 100–20 | 20–4 |
| Energy (eV) | 12–62 | 62–310 |
| Pulse length r.m.s. (fs) | 30–100 | <100 |
| Spectral width $\Delta\lambda/\lambda$ FWHM | $10^{-3}$ | $10^{-3}$ |
| Central wavelength fluctuation | $<10^{-4}$ | $<10^{-4}$ |
| Energy per pulse (µJ) | >100 | 20–100 |
| Power fluctuation (%) | <25 | <50 |
| Polarization | Linear (H/V)– circular (L/R) | Linear (H/V)– circular (L/R) |
| Repetition rate (Hz) | 10 | 10 |

the 4–20 nm (62–310 eV) range (Allaria *et al.*, 2013). The high-energy line, FEL2, differently from FEL1, is a double-stage cascade FEL based on the fresh bunch technique meaning that an external seed laser feeds the electron bunch, as for FEL1, and coherent radiation is emitted in the 20–60 nm range, which is the first stage emission. Afterwards this radiation is used for seeding a fresh part of the electron bunch that has been delayed properly by a magnetic delay line and then passes through a series of undulators. The main machine parameters and radiation properties achieved during the commissioning for both FEL1 and FEL2 are summarized in Table 1. Thanks to the seeding scheme and the combined presence of variable-gap APPLE-II undulators it is possible to scan the photon energy of the X-ray pulses continuously across the whole wavelength range, allowing the users to map the absorption–emission edges of the samples under investigation. The polarization of the emitted FEL radiation can be varied from linear (horizontal–vertical) to circular (left–right) as recently demonstrated by Allaria *et al.* (2014) and Finetti *et al.* (2014). These features make FERMI a suitable source for unprecedented ultra-fast X-ray absorption studies.

## 3. Photon transport and diagnostic system

The Photon Analysis Delivery and REduction System (PADReS) is a part of the machine from the last undulators to the end-stations (Zangrando *et al.*, 2009, 2015). Unlike the other FERMI beamlines, MagneDyn is planned to be fed by the high-energy source FEL2 from both the first stage (covering the low energies) and second stage (for the high energies). For this reason a brand new branch of PADReS will be implemented in order to measure and manipulate the photon beam down to the two planned end-stations. The layout is hereafter described (shown in Fig. 1) while the main optical components will be discussed in the following sections in detail. The beamline is planned to start inside the safety hutch, a restricted access area at the beginning of the experimental hall, by means of a gold-coated plane mirror, named $PM2a_{MD}$, located 41.4 m downstream of the last undulator. The beam will then be reflected to the on-line photon energy spectrometer, about 17 m downstream, where a small fraction of the radiation will be diffracted by one of the two diffraction gratings employed to measure on-line the

**Table 2**
MagneDyn mirrors characteristics and quality.

| Mirror | Bulk material | Bulk dimensions (mm) | Roughness r.m.s. (nm) | Tangential radius (km) | Sagittal radius (km) | Optical area (mm) | Tangential slope error r.m.s. (μrad) | Sagittal slope error r.m.s. (μrad) | Coating |
|---|---|---|---|---|---|---|---|---|---|
| PM2a$_{MD}$ | Silicon | $350 \times 60 \times 70$ | <0.3 | >30 | >30 | $300 \times 30$ | <0.5 | <5 | Au |
| KBM_H$_{MD}$ | Glass-based | $400 \times 40 \times 10$ | <0.3 | >1 | >3 | $360 \times 20$ | <0.5 | <5 | Au |
| VDM$_{MD}$ | Silicon | $410 \times 40 \times 50$ | <0.3 | >30 | >30 | $390 \times 20$ | <0.5 | <5 | Au |
| KBM_V$_{MD}$ | Glass-based | $400 \times 40 \times 10$ | <0.3 | >1 | >3 | $360 \times 20$ | <0.5 | <5 | Au |

spectral content. After the spectrometer the beam propagates freely for 14 m until the first element of the Kirkpatrick–Baez active optics system (KAOS) designed to focus the FEL light in the horizontal direction. After 1.2 m the beam is reflected by another plane mirror devoted to rise the beam vertically, named the vertical deflecting mirror (VDM$_{MD}$). About 4.3 m after the VDM$_{MD}$ the beam is finally reflected by the second element of KAOS and focused in the vertical direction inside one of the experimental end-stations. The number of mirrors/ gratings employed by the beamline will be five (six considering the two gratings) and all of them will work at 2° of grazing incidence in order to maximize the beamline transmission keeping the dimension of the substrates reasonable. The total length of the beamline, from the last undulator of FEL2 to the focal spot inside the first experimental vacuum chamber, will be around 80 m. In the following sections each optical element as well as its features will be described in detail.

## 3.1. Plane mirrors

As described in the previous section, the beamline will employ two plane mirrors. The first plane mirrors PM2a$_{MD}$ and VDM$_{MD}$ (placed 32.2 m downstream of PM2a$_{MD}$) will collect the whole incoming beam. For both mirrors the tangential and sagittal radii of curvature will be more than 30 km in order to prevent unwanted focusing effects. The surface quality is within the standards of the other mirrors employed at the other FERMI beamlines in order to guarantee the preservation of the wavefront and limit the possible aberrations of the photon beam. The substrates have a gold

coating with a negligible surface roughness in order to avoid scattering effects of the reflected light that cannot be focused properly. In Table 2 all the mirror parameters are summarized.

## 3.2. On-line photon energy spectrometer

After PM2a$_{MD}$ the photon beam will impinge over the on-line photon energy spectrometer. The working scheme is similar to that of the already installed PRESTO (Svetina *et al.*, 2011, 2016) and is composed of two diffraction gratings, one for the low-energy range and one for the high-energy range. The zeroth order of diffraction will be delivered almost unperturbed to the users (*i.e.* the full FEL photon beam from the source) while the first–second order of diffraction will be used for the characterization of the spectral content. So as not to perturb the photon beam, the substrates will be flat while the gratings will be variable line spacing (VLS) meaning that the groove density is not constant along the substrate. In this way the diffraction angles are different along the tangential direction of the grating with consequent focusing into the detector. No entrance nor exit slits will be used. Since the incidence angle is constant (2°) the focal displacement is a function of the radiation wavelength, forming the so-called focal curve. For this reason the detector will be mounted over an X–Y translation stage allowing the diffracted spot to be followed. The two gratings will both have a 200 mm × 25 mm × 40 mm (L × W × H) fused silica flat substrate with a clear aperture of 180 mm × 20 mm while just the central part will be ruled with a dimension of 60 mm × 17 mm. This is because just a small fraction of the incoming photon beam is sufficient to
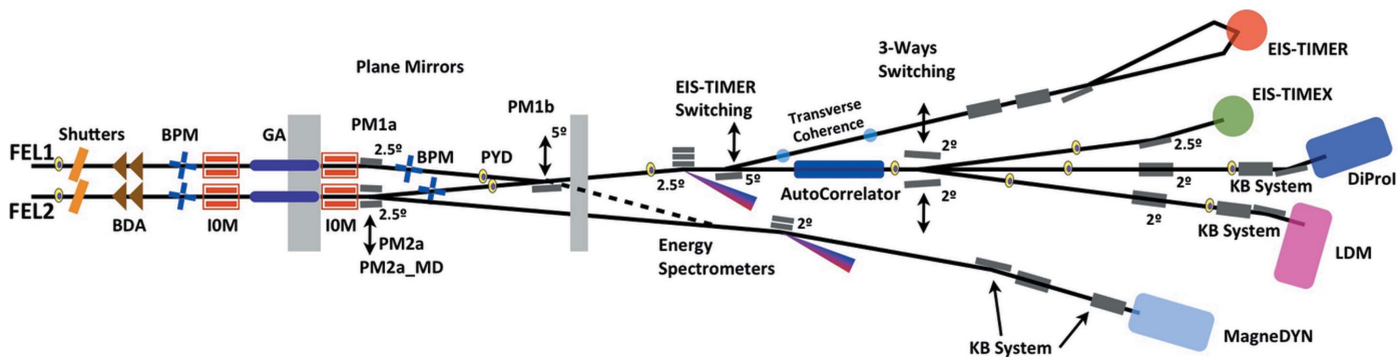
**Figure 1**
Layout of the PADReS system and end-station at FERMI. Left to right: shutters, beam-defining apertures (BDA), beam position monitors (BPM), intensity monitors (I0M), gas absorber (GA), four plane mirrors inside the safety hutch (PM1a, PM1b, PM2a, PM2a$_{MD}$), Ce:YAG screens, photodiode-YAG-diagnostics (PYD). At the beginning of the experimental hall the photon energy spectrometers, the auto-correlator delay-creator (AC/DC) are present followed by the five beamlines with their refocusing systems.

measure the spectral properties of the FEL while maximizing the beamline transmission. For the same reason the groove profiles have been chosen to be laminar in order to have a relatively low efficiency (between 0.4% and 4%) at the first order of diffraction but with sufficient at the second (between 0.5% and 2%).

The low-energy grating (LE) will cover the wavelength range from 6.75 nm up to 60.5 nm (20.5–185 eV) and will have a 30 nm single layer of coating made of amorphous carbon (a-C). The high-energy grating (HE) will cover the wavelength range from 2.1 nm up to 9.6 nm (130–590 eV) by using the first order of diffraction and will measure down to 1.05 nm (1180 eV) using the second one. As for the mirrors, the spectrometer's substrates will have small tangential (below 0.5 µrad r.m.s.) and sagittal (below 5 µrad r.m.s.) slope errors with a residual radius of curvature greater than 30 km and a micro-roughness below 0.4 nm r.m.s. These specifications will guarantee the preservation of the wavefront, the transverse spot quality as well as the minimization of the scattered light.

The gratings' VLS coefficients have been calculated using the theoretical formulas (Peatman, 1997) at first and have then been optimized with ray-tracing simulation (Cerrina *et al.*, 1994). In Table 3 all the main parameters of the gratings are summarized. The spectrometer performances in terms of spot

**Table 3**
Main parameters of the gratings composing the photon energy spectrometer.

The coefficients $D_i$ have been chosen in order to focus the diffracted radiation over the detector while the profile parameters and the coatings have been fixed considering the absolute efficiency of the gratings.

|  | LE | HE |
|---|---|---|
| Wavelength range (nm) | 6.75–60.5 | 1.05–6.75 |
| Energy range (eV) | 20.5–185 | 130–1180 |
| Groove density $D_0$ (grooves mm$^{-1}$) | 600 | 3750 |
| $D_1$ (grooves mm$^{-2}$) | $4.20 \times 10^{-1}$ | 2.6 |
| $D_2$ (grooves mm$^{-3}$) | $2.10 \times 10^{-4}$ | $1.30 \times 10^{-3}$ |
| $D_3$ (grooves mm$^{-4}$) | $9.50 \times 10^{-11}$ | $5.90 \times 10^{-10}$ |
| Groove profile | Laminar | Laminar |
| Groove height (nm) | 10 | 4 |
| Groove ratio ($w/d$) | 0.7 | 0.7 |
| Coating / thickness (nm) | a-C / 30 | Au / 30 |

size and resolving power have been simulated by means of ray-tracing simulations adopting the Rayleigh criteria for the latter. Thanks to the high number of illuminated grooves the theoretical resolving power of the system is expected to be high, *i.e.* around $10^5$ over the whole wavelength range (Fig. 2; spots: top, HE at 6.25 nm; bottom, LE at 20 nm. Fig. 3: calculated resolving powers).

The grating's efficiencies have been calculated with the *REFLEC* (Schäfers, 1996) and *LUMNAB* (Nevière *et al.*, 1974) codes for both the diffracted and transmitted beams considering the groove profile and coating of both gratings. For the LE the relative efficiency is expected to be between 0.5% and 3% for both the first and second orders of diffraction. The HE grating will have an efficiency between 0.8% and 2% at the first order while the second order will be around 0.5%. The transmitted beam (zeroth order of diffraction) is expected to have an intensity slightly lower than if a regular mirror would have been used (reflectivity) as shown in Fig. 4. In order to measure the spectral content, the diffracted FEL radiation will be focused onto a dedicated movable detector able to follow the focal curve displacement. The detector is
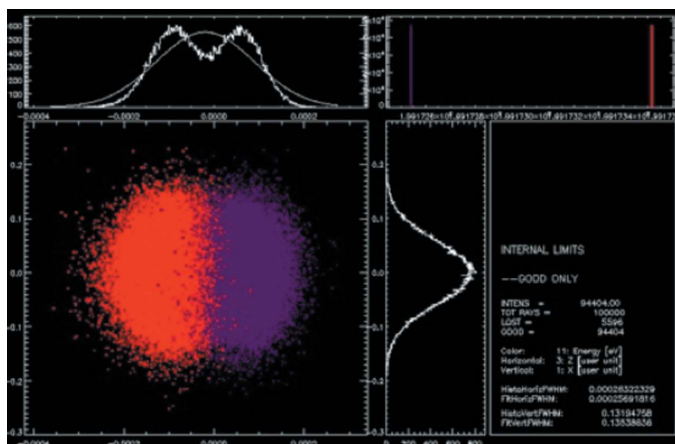


**Figure 2**
Simulated spots at the detector with *SHADOW* code at 6.25 nm (top) and 20 nm (bottom) wavelength radiation.
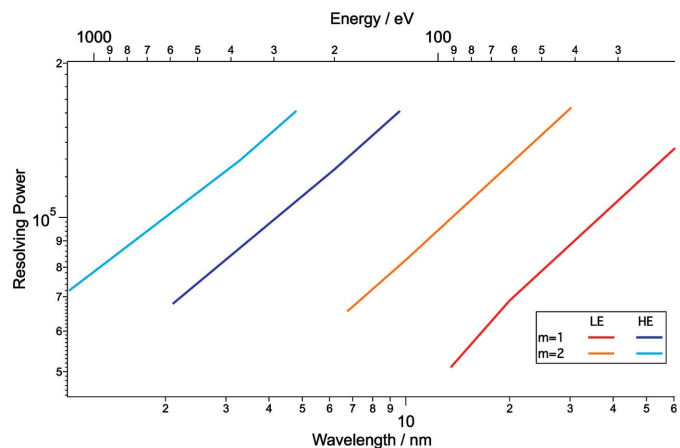


**Figure 3**
Calculated resolving power of both gratings using the Rayleigh criteria. The various colors correspond to different orders of diffraction: red (first, LE), orange (second, LE), blue (first, HE) and magenta (second, HE).
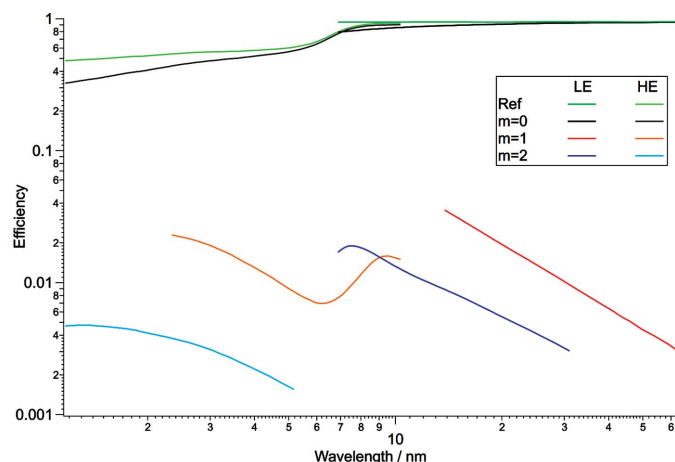
**Figure 4**
Grating efficiency at the zeroth ($m = 0$, black/grey), first ($m = 1$, red/orange) and second ($m = 2$, blue/azure) orders of diffraction for the low-energy (LE) and high-energy (HE) gratings over the whole FERMI FEL2 wavelength range. The intensity used by the spectrometer is much lower than the total radiation delivered to the users (zeroth order, $m = 0$) and is slightly lower than the purple dotted lines corresponding to the reflectivity of a single mirror with the same coating and incidence angle as the gratings.



**Figure 5**
Sketch of the active plane-elliptical mirror composing KAOS. The thin substrate is bent by a set of two pushers acting on the mirror's holder. Applying unequal forces it is possible to change the shape of the mirror leading to the desired profile.

foreseen to be a YAG screen (in vacuum) coupled with a visible CCD camera (in air), as for PRESTO. This solution allows a high resolving power to be maintained in air conditions as well as the possibility of a fast replacement of the YAG screen in the case of damage due to the radiation.

### 3.3. KAOS

The focusing section, named KAOS, will be composed of a set of two active plane-elliptical mirrors mounted in the Kirkpatrick–Baez (KB) (Kirkpatrick & Baez, 1948) configuration similar to the already adopted solution (Raimondi *et al.*, 2013, 2014). The KB geometry allows the vertical and horizontal focusing to be decoupled and the available substrates have a much higher surface quality compared with the ellipsoidal mirrors. The reasons why the beamline needs active mirrors are the following:

(i) Sources: end-stations and wavefront correction. As described previously, FEL2 provides two photon beams: the low-energy beam from the first stage (down to 20 nm) and the high-energy beam from the second stage. These stages are separated by about 28.8 m meaning that for a fixed focal length the beams cannot both be focused properly.

(ii) Two experimental end-stations: a magnet and a RIXS about 1 m apart. In order to move the focal spot inside the working chamber the mirrors have to be of variable focal length.

(iii) Wavefront control: the possibility to change the mirror shape will allow the wavefront of the photon beam to be controlled.

The active mirrors will have a flat substrate of fused silica with an overall dimension of 400 mm × 40 mm × 10 mm (L × W × H), *i.e.* much thinner than the regular mirrors employed along the beamlines. The clear aperture will be 360 mm ×
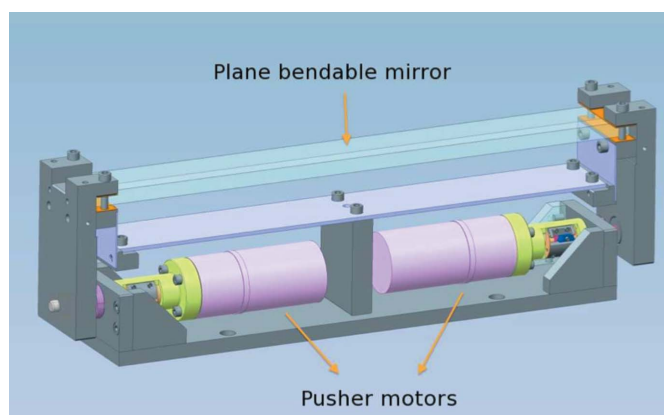
20 mm with a residual radius of curvature above 3 km within 70 mm area, below 0.5 µrad r.m.s. and 5 µrad r.m.s. for the tangential and sagittal slope errors and with a micro-roughness below 0.3 nm r.m.s. The relaxed constrains of the residual radius of curvature is due to the fact that the mirrors are thin because they have to be deformable. Both mirrors will be coated with a single layer made of 30 nm of gold. The mirrors will be mounted on a dedicated holder custom-designed in such a way that only the sides are clamped while the central part is free to be bent. By applying two unequal forces with a set of pushers over the sides it will be possible to change the mirror tangential shape according to the user needs. Each pusher will be composed of a stepper motor coupled with a piezo-electric actuator: the former for the coarse mirror shape, the latter for the fine optimization. A schematic of the system is shown in Fig. 5.

## 4. Beamline performances

The source has been modeled as a geometric Gaussian source with the parameters measured during the commissioning of FEL2, such as source size and angular divergence for both first and second stages, and then propagated along the mirrors composing the beamline down to the two end-stations. The presence of the slope errors, which affect the spot quality and wavefront at the focus, has been taken into account as well as the finite size of the mirrors/gratings that cause diffraction and geometrical losses with consequent drop of the total beamline transmission. The results are described in detail in the following subsections.

### 4.1. Beamline transmission and polarization

Considering the presence of the various coatings employed and the incidence angles, the beamline transmission has been calculated with particular attention to the effect on the polarization. In fact, one of the key elements for studying the magnetic properties of the materials is the presence of pure

circular polarized light. Since the beamline will employ grazing-incidence single-layered mirrors, three of those working in the horizontal direction and two in the vertical, the degree of polarization of the radiation is expected to be mostly conserved. However, for the longer wavelengths (above 30 nm) a small effect will be present leading to a slightly elliptical polarized light when circular polarized radiation will be provided by the machine. Moreover, the presence of APPLE-II undulators allows the polarization of the emitted radiation to be controlled. In particular, it can be generated with an ellipsoidal polarization in such a way that the beamline itself makes it circular at the experimental end-stations.

The beamline transmission has been maximized using a grazing-incident geometry for all the mirrors (2° of grazing incidence) employing a proper gold coating over the substrates (but for the LE grating which is a-C). It ranges from 70% for the long wavelengths (7–60 nm, 21–177 eV), between 10% and 20% for the range 3–6 nm (207–413 eV), and drops down to 7% for the very short wavelengths (around 1 nm, 1240 eV).

In addition to the mirror's reflectivity, another important cause of loss of beamline transmission is the geometrical losses. These are due to the finite size of the mirrors as well as the presence of apertures as a function of the incoming wavelength. In fact the photon beam divergence is linearly correlated to the wavelength meaning that the longer the wavelength of the radiation the more the transverse spot will enlarge along the beamline. Their effect will be negligible at wavelengths below 20 nm (62 eV) where the beam is confined within the length of the mirrors. At longer wavelengths, for radiation emitted in the first stage, the geometrical cuts become relevant with transmission going from 87% at 30 nm (41 eV) down to 45% at 60 nm (21 eV). The overall beamline transmission is shown in Fig. 6 having taken into account both reflectivity and geometrical losses in the whole FEL2 range. Considering a photon flux at the source of about 100 μJ, we
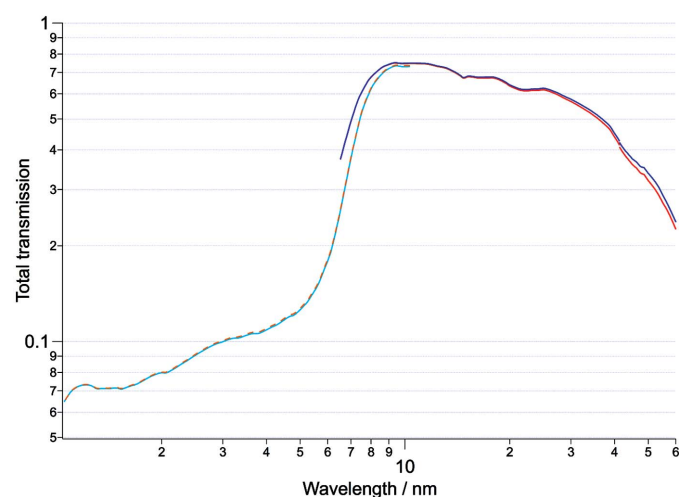
expect to obtain an intensity at the sample of the order of 58 μJ at 30 nm and 20 μJ at 6 nm. These intensities will correspond to a fluence at the sample of the order of $2.5 \times 10^{12}$ W cm$^{-2}$ and $8.2 \times 10^{11}$ W cm$^{-2}$, respectively. Of course the photon beam can be attenuated by means of a set of dedicated solid state filters (such as aluminium, zirconium, palladium, *etc.*) and/or by using the PADReS gas attenuator already operative. Moreover, the beam size can be easily enlarged by acting on the KAOS mirrors shape in order to drop the fluence even more if needed.

## 4.2. Focal spot

The only difference between the already operative KAOS system at DIPROI or LDM and the MagneDyn KAOS will be the fact that the two mirrors will not be in cascade (in series) but will be 5.5 m apart, with the VDM$_{MD}$ in between. As a consequence the demagnification factor of the two mirrors will be different with a small focus in the vertical direction and a wider one in the horizontal. In particular the horizontal KB will demagnify the source by a factor of 10 while this number rises up to 39 for the vertical KB. This means that the focused beam will not be circular but ellipsoidal with an average ratio between the two axes of about 4. This will not be a problem since inside both experimental chambers a horizontal entrance slit will be used, limiting the beam dimension in the vertical direction allowing the horizontal component to pass unperturbed. The spots at the focus have been simulated considering the whole beamline system (mirrors/gratings) by ray tracing (Cerrina *et al.*, 1994) as well as wavefront propagation simulations (Raimondi & Spiga, 2010, 2015; Spiga & Raimondi, 2014). The source has been modelled as a Gaussian distribution with a transverse dimension of 125 μm $\sigma$ and a divergence following the relation $\sigma'_{\mu rad} = k\lambda_{nm}$, with $k = 1.25$ for the FEL2 first stage and 1.5 for the FEL2 second stage. The results are in agreement with both approaches (both for some diffraction effect due to the finite size of the mirrors) and the spots are expected to be 14 μm × 3.5 μm (H × V) FWHM at the electromagnet chamber and 16 μm × 5.3 μm FWHM at RIXS. In Fig. 7 some selected simulated spots at 20 nm (62 eV) are shown inside the electromagnet end-station having used ray-tracing (left) and wavefront propagation (right) approaches. In the case of very long wavelengths generated in the first stage, where the divergence is higher, the diffraction effects cause the spot to be wider in the horizontal direction, leading to a spot of up to 30 μm FWHM at 60 nm (21 eV).

## 5. Conclusion and outlooks

MagneDyn is expected to be assembled at the beginning of 2016 in a basic configuration consisting of all the mirrors (plane and KBs) without the photon energy spectrometer. Within 2016 the beamline will be commissioned and the gratings, as well as the whole spectrometer mechanical system, will be purchased. In the future the 14 m free space between the spectrometer and the first focusing mirror (KB$_H$) will be
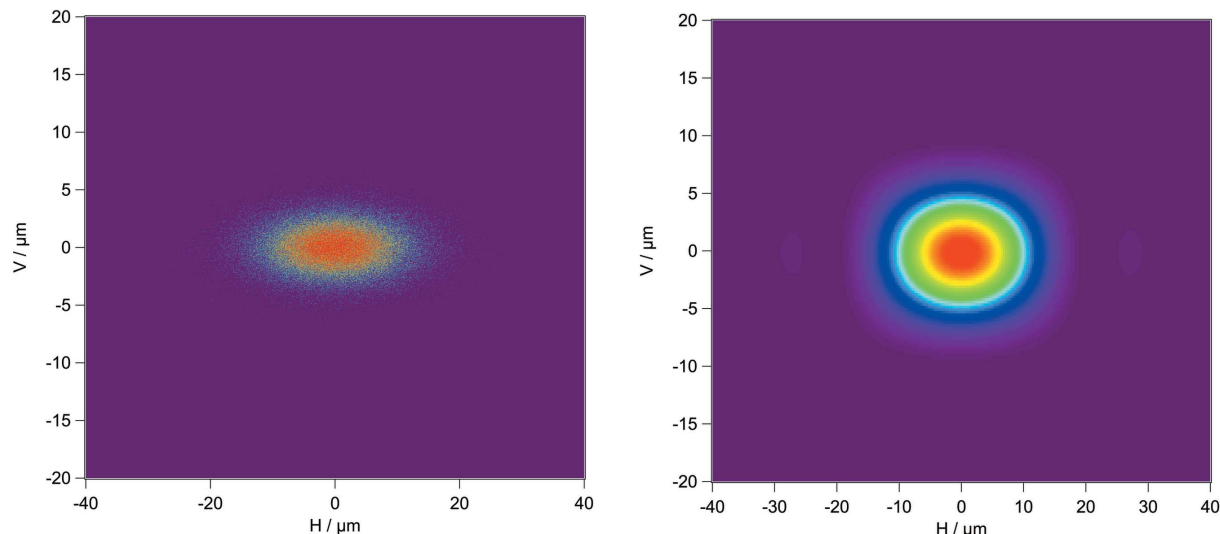


**Figure 6**
Total beamline transmission for horizontal (blue/azure) and vertical (red/orange) linear polarized light. The simulations have taken into account the mirrors/gratings reflectivity/efficiency as well as the geometrical losses due to the finite size of the mirrors.

**Figure 7**
Comparison between simulated spots at the focus inside the electromagnet end-station at 20 nm (62 eV). The ray-tracing results (left) are in good agreement with the wavefront propagation simulations (right) but for some negligible diffraction effects. The spot size is expected to be around 14 μm × 3.5 μm (H × V) FWHM.

filled with a wavefront split-and-delay line similar to the already installed auto-correlator/delay-creator (AD/DC) (Zangrando *et al.*, 2015). Another possible upgrade will be merging the low-energy source FEL1 with the beamline. This will extend the working energy range up to 100 nm with higher intensities.

## Acknowledgements

## References

Allaria, E., Appio, R., Badano, L., Barletta, W. A., Bassanese, S., Biedron, S. G., Borga, A., Busetto, E., Castronovo, D., Cinquegrana, P., Cleva, S., Cocco, D., Cornacchia, M., Craievich, P., Cudin, I., D'Auria, G., Dal Forno, M., Danailov, M. B., De Monte, R., De Ninno, G., Delgiusto, P., Demidovich, A., Di Mitri, S., Diviacco, B., Fabris, A., Fabris, R., Fawley, W., Ferianis, M., Ferrari, E., Ferry, S., Froehlich, L., Furlan, P., Gaio, G., Gelmetti, F., Giannessi, L., Giannini, M., Gobessi, R., Ivanov, R., Karantzoulis, E., Lonza, M., Lutman, A., Mahieu, B., Milloch, M., Milton, S. V., Musardo, M., Nikolov, I., Noe, S., Parmigiani, F., Penco, G., Petronio, M., Pivetta, L., Predonzani, M., Rossi, F., Rumiz, L., Salom, A., Scafuri, C., Serpico, C., Sigalotti, P., Spampinati, S., Spezzani, C., Svandrlik, M., Svetina, C., Tazzari, S., Trovo, M., Umer, R., Vascotto, A., Veronese, M., Visintini, R., Zaccaria, M., Zangrando, D. & Zangrando, M. (2012). *Nat. Photon.* **6**, 699–704.
Allaria, E., Castronovo, D., Cinquegrana, P., Craievich, P., Dal Forno, M., Danailov, M. B., D'Auria, G., Demidovich, A., De Ninno, G., Di Mitri, S., Diviacco, B., Fawley, W. M., Ferianis, M., Ferrari, E., Froehlich, L., Gaio, G., Gauthier, D., Giannessi, L., Ivanov, R., Mahieu, B., Mahne, N., Nikolov, I., Parmigiani, F., Penco, G., Raimondi, L., Scafuri, C., Serpico, C., Sigalotti, P., Spampinati, S., Spezzani, C., Svandrlik, M., Svetina, C., Trovo, M., Veronese, M., Zangrando, D. & Zangrando, M. (2013). *Nat. Photon.* **7**, 913–918.
Allaria, E., Callegari, C., Cocco, D., Fawley, W. M., Kiskinova, M., Masciovecchio, C. & Parmigiani, F. (2010). *New J. Phys.* **12**, 075002.
Allaria, E., Diviacco, B., Callegari, C., Finetti, P., Mahieu, B., Viefhaus, J., Zangrando, M., De Ninno, G., Lambert, G., Ferrari, E., Buck, J., Ilchen, M., Vodungbo, B., Mahne, N., Svetina, C., Spezzani, C., Di Mitri, S., Penco, G., Trovó, M., Fawley, W. M., Rebernik, P. R., Gauthier, D., Grazioli, C., Coreno, M., Ressel, B., Kivimäki, A., Mazza, T., Glaser, L., Scholz, F., Seltmann, J., Gessler, P., Grünert, J., De Fanis, A., Meyer, M., Knie, A., Moeller, S. P., Raimondi, L., Capotondi, F., Pedersoli, E., Plekan, O., Danailov, M. B., Demidovich, A., Nikolov, I., Abrami, A., Gautier, J., Lüning, J., Zeitoun, P. & Giannessi, L. (2014). *Phys. Rev. X*, **4**, 041040.
Battiato, M., Carva, K. & Oppeneer, P. M. (2010). *Phys. Rev. Lett.* **105**, 027203.
Beaurepaire, E., Merle, J.-C., Daunois, A. & Bigot, J.-Y. (1996). *Phys. Rev. Lett.* **76**, 4250–4253.
Bigot, J.-Y., Vomir, M. & Beaurepaire, E. (2009). *Nat. Phys.* **5**, 515–520.
Boeglin, C., Beaurepaire, E., Halté, V., López-Flores, V., Stamm, C., Pontius, N., Dürr, H. A. & Bigot, J.-Y. (2010). *Nature (London)*, **465**, 458–461.
Carpene, E., Mancini, E., Dallera, C., Brenna, M., Puppin, E. & De Silvestri, S. (2008). *Phys. Rev. B*, **78**, 174422.
Cerrina, F., Welnak, C., Chen, G. J. & Sanchez del Rio, M. (1994). *SHADOW PRIMER.* Center for X-ray Lithography, University of Wisconsin, Wisconsin, USA.
Cinchetti, M., Sánchez Albaneda, M., Hoffmann, D., Roth, T., Wüstenberg, J.-P., KrauSSSSs, M., Andreyev, O., Schneider, H. C., Bauer, M. & Aeschlimann, M. (2006). *Phys. Rev. Lett.* **97**, 177201.
Finetti, P., Allaria, E., Diviacco, B., Callegari, C., Mahieu, B., Viefhaus, J., Zangrando, M., De Ninno, G., Lambert, G., Ferrari, E., Buck, J., Ilchen, M., Vodungbo, B., Mahne, N., Svetina, C., Spezzani, C., Di Mitri, S., Penco, G., Trovò, M., Fawley, W. M., Rebernik, P., Gauthier, D., Grazioli, C., Coreno, M., Ressel, B., Kivimäki, A., Mazza, T., Glaser, L., Scholz, F., Seltmann, J., Gessler, P., Grünert, J., De Fanis, A., Meyer, M., Knie, A., Moeller, S. P., Raimondi, L., Capotondi, F., Pedersoli, E., Plekan, O., Danailov, M., Demidovich, A., Nikolov, I., Abrami, A., Gautier, J., Lüning, J., Zeitoun, P. & Giannessi, L. (2014). *Proc. SPIE*, **9210**, 92100K.
Kirilyuk, A., Kimel, A. V. & Rasing, T. (2010). *Rev. Mod. Phys* **82**, 2731–2784.
Kirkpatrick, P. & Baez, A. V. (1948). *J. Opt. Soc. Am.* **38**, 766–773.
Koopmans, B., Malinowski, G., Dalla Longa, F., Steiauf, D., Fähnle, M., Roth, T., Cinchetti, M. & Aeschlimann, M. (2010). *Nat. Mater.* **9**, 259–265.

Koopmans, B., Ruigrok, J., Dalla Longa, F. & De Jonge, W. (2005). *Phys. Rev. Lett.* **95**, 267207.

La-O-Vorakiat, C., Siemens, M., Murnane, M. M., Kapteyn, H. C., Mathias, S., Aeschlimann, M., Grychtol, P., Adam, R., Schneider, C. M., Shaw, J. M., Nembach, H. & Silva, T. J. (2009). *Phys. Rev. Lett.* **103**, 257402.

Mueller, B. Y., Baral, A., Vollmar, S., Cinchetti, M., Aeschlimann, M., Schneider, H. C. & Rethfeld, B. (2013). *Phys. Rev. Lett.* **111**, 167204.

Nevière, M., Vincent, P. & Petit, R. (1974). *Nouv. Rev. Opt.* **5**, 65.

Peatman, W. B. (1997). *Gratings, Mirrors and Slits: Beamline Design for Soft X-ray Synchrotron Radiation Sources.* New York: Gordon and Breach.

Raimondi, L. & Spiga, D. (2010). *Proc. SPIE*, **7732**, 7732.

Raimondi, L. & Spiga, D. (2015). *Astron. Astrophys.* **573**, A17.

Raimondi, L., Svetina, C., Mahne, N., Cocco, D., Capotondi, F., Pedersoli, E., Kiskinova, M., Keitel, B., Brenner, G., Plönjes, E., Mey, T., Mann, K. & Zangrando, M. (2013). *Proc. SPIE*, **8848**, 88480B.

Raimondi, L., Svetina, C., Mahne, N., Cocco, D., Capotondi, F., Pedersoli, E., Manfredda, M., Kiskinova, M., Keitel, B., Brenner, G., Plönjes, E., Mey, T., Mann, K. & Zangrando, M. (2014). *Proc. SPIE*, **9208**, 920804.

Schäfers, F. (1996). BESSY Technical Report 202/96. BESSY, Berlin, Germany.

Spiga, D. & Raimondi, L. (2014). *Proc. SPIE*, **9209**, 92090E.

Stamm, C., Kachel, T., Pontius, N., Mitzner, R., Quast, T., Holldack, K., Khan, S., Lupulescu, C., Aziz, E. F., Wietstruk, M., Dürr, H. A. & Eberhardt, W. (2007). *Nat. Mater.* **6**, 740–743.

Stohr, J. & Siegmann, H. C. (2006). *Magnetism: From Fundamentals to Nanoscale Dynamics. Magnetism: From Fundamentals to Nanoscale Dynamics, Springer Series in Solid-State Physics*, Vol. 152. Berlin: Springer.

Svetina, C., Abrami, A., Cudin, I., Fava, C., Gerusina, S., Gobessi, R., Rumiz, L., Sostero, G., Zangrando, M. & Cocco, D. (2011). *Proc. SPIE*, **8139**, 81390J.

Svetina, C., Cocco, D., Mahne, N., Raimondi, L., Ferrari, E. & Zangrando, M. (2016). *J. Synchrotron Rad.* **23**, 35–42.

Tudosa, I., Stamm, C., Kashuba, A. B., King, F., Siegmann, H. C., Stöhr, J., Ju, G., Lu, B. & Weller, D. (2004). *Nature (London)*, **428**, 831–833.

Wietstruk, M., Melnikov, A., Stamm, C., Kachel, T., Pontius, N., Sultan, M., Gahl, C., Weinelt, M., Dürr, H. A. & Bovensiepen, U. (2011). *Phys. Rev. Lett.* **106**, 127401.

Yu, L. Y. (1991). *Phys. Rev. A*, **44**, 5178–5193.

Zangrando, M., Abrami, A., Bacescu, D., Cudin, I., Fava, C., Frassetto, F., Galimberti, A., Godnig, R., Giuressi, D., Poletto, L., Rumiz, L., Sergo, R., Svetina, C. & Cocco, D. (2009). *Rev. Sci. Instrum.* **80**, 113110.

Zangrando, M., Cocco, D., Fava, C., Gerusina, S., Gobessi, R., Mahne, N., Mazzucco, E., Raimondi, L., Rumiz, L. & Svetina, C. (2015). *J. Synchrotron Rad.* **22**, 565–570.